Forearc high uplift by deep crustal flow during growth of the Anatolian margin

David Fernández-Blanco[1], Giovanni Bertotti[1], and Sean Willett[2]

[1] Department of Geoscience and Engineering, Faculty of Civil Engineering and Geosciences, Delft, University of Technology, Stevinweg 1, 2628CN, Delft, the Netherlands
geo.david.fernandez@gmail.com
[2] Geological Institute, Swiss Federal Institute of Technology, 8092 Zurich, Switzerland.

Abstract

We present a model for the dynamic formation of the forearc high of southern Anatolia where sedimentation in the forearc basin leads to thermally-activated deformation in the lower crust. Our thermo-mechanical models demonstrate that forearc sedimentation increases the temperature of the underlying crust by "blanketing" the heat flux and increasing Moho depth. Deformation switches from frictional to viscous with a higher strain rate due to increased temperature. Viscous deformation changes large-wavelength subsidence into coeval, short-wavelength uplift and subsidence. Forearc highs are intrinsic to accretionary wedges and can grow dynamically and non-linearly at rates dependent on sediment accretion, sedimentation and temperature. The mechanism explains Neogene upper-plate strain, vertical motions and first-order stratigraphic relationships in Central Cyprus and across the plateau margin in South Turkey. This system is analogous to forearc highs in other mature accretionary margins, like Cascadia, the Lesser Antilles or Nankai.

keywords: forearc high; uplift; subduction wedge; subduction zone; plateau margin; Central Anatolian Plateau

Introduction

Climatic and geodynamic processes are the first-order drivers of topography in orogenic plateaus and plateau margins. However, mechanisms for detailed patterns of uplift in orogenic plateau systems, such as Himalaya-Tibet and Puna-Altiplano (e.g., Molnar, 1984; Allmendinger et al., 1997; Strecker et al., 2009) remain diverse and difficult to generalize. This is also true for the history of topography growth of the Central Anatolia Plateau and its margins. While continental delamination (Bartol and Govers, 2014) or lithospheric drip (Göğüş et al., 2017) may sustain Central Anatolia low relief at ~1 km, its plateau margins are geodynamically different; transpressional orogenic uplift may have formed the northern margin (Yildirim et al., 2011) whereas the southern margin is strongly influenced by the Cyprus subduction zone to the south.

The formation mechanism of the southern margin of the Central Anatolian Plateau (SCAP), at a forearc high location of the Central Cyprus subduction zone (Fig. 1), is of particular interest, as vertical tectonic motions prior and during its growth occurred in the absence of regional accommodating faults. Middle and Late Miocene subsidence, that broadened a forearc basin spanning from the present SCAP to Central Cyprus, was followed by Late Miocene and younger short-wavelength tectonic motions, i.e. uplift of South Turkey and coeval seaward subsidence (Walsh-Kennedy et al., 2014). At present, Late Miocene shallow marine rocks outlining the SCAP flexural monocline (Fernández-Blanco et al., 2018) lay at ~-2 km depth in the Cilicia Basin (Aksu et al., 2005) and at ~2 km elevation in the modern Central Taurides (Cosentino et al., 2012).

Several geodynamic scenarios are suggested to explain SCAP uplift. Epeirogenic surface uplift due to shallow slab break-off (e.g., Schildgen et al., 2014) is compatible with stratigraphic and paleontological records (Cosentino et al., 2012) and the thinned Central Anatolian lithosphere inferred from seismic tomography (Mutlu and Karabulut,

2011). However, the sharp boundaries and short wavelength between margin uplift and seaward subsidence (Fernández-Blanco et al., 2018) differs from large wavelength motions expected from epeirogenic uplift (e.g., Göğüş and Pysklywec, 2008). Also, the presence of the African slab (e.g., Abgarmi et al., 2017) and the thick Anatolian mantle lithosphere (e.g., Delph et al., 2017) under the modern Central Taurides suggest that other mechanisms, such as crustal thickening (Fernández-Blanco et al., 2018; Meijers et al., 2018), must have played a role in uplifting the plateau margin. In this paper, we demonstrate that a mechanism of deep crustal thickening by thermally-activated viscous flow, as proposed by Fuller et al. (2006), is consistent with the spatial and temporal patterns of subsidence and uplift of the plateau margin.

Forearc deformation of an orogenic wedge (Platt, 1986; Willett et al., 1993), where deep-seated crustal flow results in forearc high uplift has been proposed for the Lesser Antilles, Cascadia and other accretionary margins (Pavlis and Bruhn, 1983), and is potentially preceded by the development of a forearc basin that is later fragmented by the uplift of the high (McNeill et al., 2000). If the forearc basin forms as a negative-alpha basin, stabilizing the underlying wedge (Willett and Schlunegger, 2010), basin growth may promote ductile deformation in the lower crust, and a late stage uplift of the forearc high (Fuller et al., 2006). This thermo-mechanical interplay can provide an important uplift mechanism.

Here, we explore the role of wedge-top sedimentation on forearc dynamics for conditions applicable to the Cyprus-Anatolia margin. We use coupled thermo-mechanical numerical models with visco-plastic attributes constrained to be consistent with the geology of the Central Cyprus subduction margin. An important transition emerges in these models as accretionary growth and sediment deposition produce a "thermal blanketing" effect restricting heat flux from underneath the forearc basin and leading to thermal weakening of the upper plate. In this context, forearc highs grow

dynamically and non-linearly as integral parts of accreting wedges, often seaward of any continental backstop. Our simulations reproduce SCAP growth as forearc high of the Central Cyprus forearc.

Central Cyprus subduction and its forearc

Along the Central Cyprus subduction zone (at 33°30'E longitude), the African lithosphere under-thrusts northwards below the Anatolian plate (Fig. 1B). Overriding lithosphere and crust have maximum thicknesses of ~110 km and ~45 km at the contact with the slab, below the modern Central Taurides, and thin northwards in Central Anatolia down to ~85 km and ~35 km (Fig. 1B). This geometry suggests thickening of the Anatolian plate in relation with subduction. Find details on the data used and our interpretation for sections in Fig. 1B and 1C in Data Repository DR1.

Compressional, regional-scale structures along the Cyprus forearc become older northwards (Fig. 1C). South-verging thrusts rooted in the subduction megathrust are presently active in the trench and pass northwards into thrust culminations covered by Quaternary and Pleistocene rocks in North Cyprus (Fig. 1C-b). The north-verging thrust in Central Cilicia Basin is mid-Pliocene (Fig. 1C-c). In the Cilicia Basin northern margin, Messinian salts pinch out where Pliocene rocks overlay an erosional contact with Miocene rocks, attesting to pre-Pliocene uplift. Uplifted Miocene rocks in the Mut Basin suggest a flexural monocline with no Miocene or younger surface-reaching thrusts (Fig. 1D-d). These regional-scale structures result in structural highs that bound basins or basin sectors and compartmentalize the Cyprus forearc at distances of ~40-50 km (Fig. 1C, *a* to *f*). A basement high and the Kyrenia Range bound the Messaoria Basin (*a* to *b*, ~40 km), and a deep-rooted thrust system in the center of the Cilicia Basin (*c*) set two sub-basins with similar length (~50 km). Basement highs discriminating sectors within the Mut Basin (*d, e, f*) also appear at similar distances. These observations are consistent with strain accommodation lead by accretion in the Central Cyprus subduction margin.
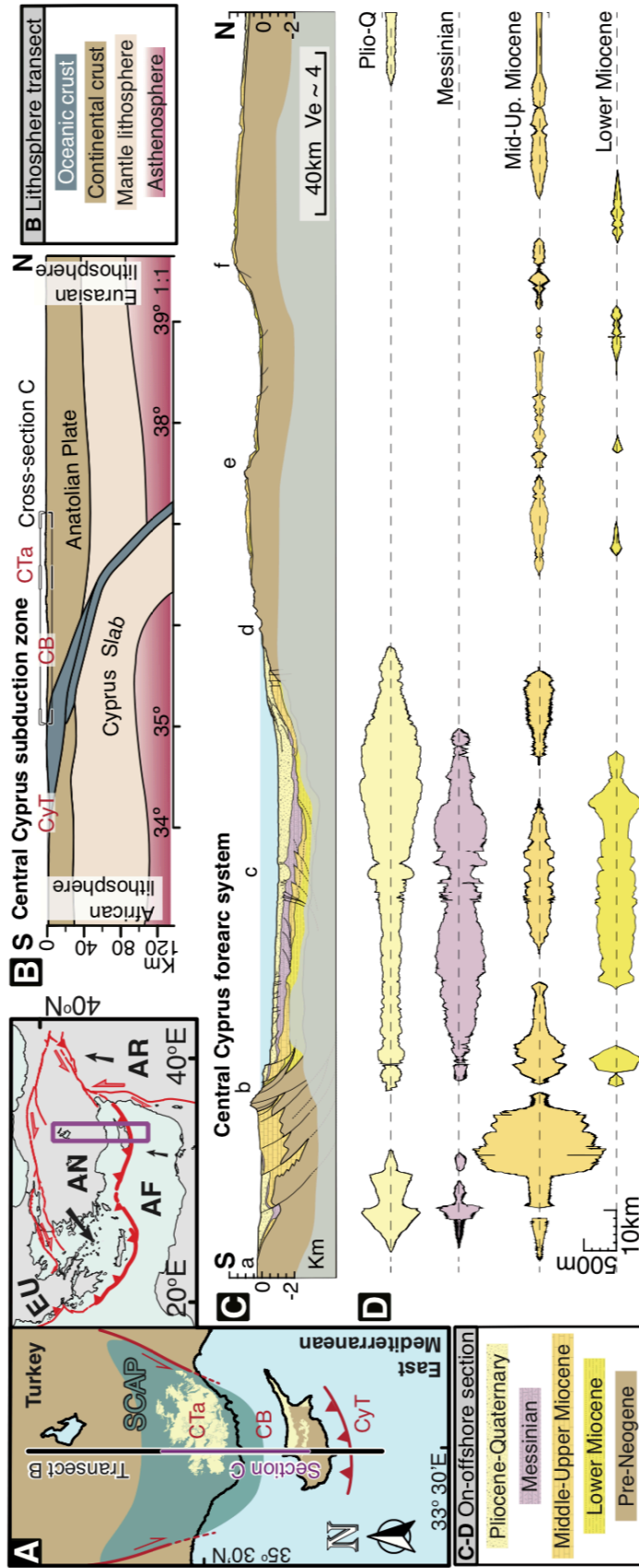
Figure 1. A: Central Cyprus subduction zone and surrounding tectonic frame, with location of B and C transects. Neogene rocks outcropping inland in yellow. EU, AN, AF, AR = Eurasian, Anatolian, African and Arabian plate; SCAP = Southern margin of the Central Anatolian Plateau; CTa = Central Taurus; CB = Cilicia Basin; CyT = Cyprus trench. B: Lithospheric-scale transect along the Central Cyprus subduction (~650 km at 33°30'E) at real scale. C: Upper crustal transect along the Central Cyprus forearc (~300 km at 33°30'E), exaggerated ~4 times in the vertical. Lowercase letters "a" to "f" show rough location of structural highs bounding basinal sectors of similar lengths. Suppl. Material in DR1 for data used and interpretation. D: Thicknesses of main stratigraphical units along the transect and their age.

Basin infill is regionally continuous until the Messinian and deposited exclusively in seaward sectors of the Central Cyprus forearc thereafter (Fig. 1C, D). After terrestrial sedimentation, pre-Messinian Miocene neritic limestones were deposited atop pre-Miocene basement (Cosentino et al., 2012). These shallow water rocks are continuous from Central Turkey to the Messaoria Basin, where the pre-Messinian basin thins to the south. Since the Messinian, rocks deposited seaward off the present Turkish coast, with basin depocenters occurring at northward locations at younger ages (Fig. 1C, D). This suggests that there was a protracted, large-wavelength subsidence of a wide forearc basin prior to the Messinian, followed by younger surface uplift of the modern Central Taurides with concomitant, counteracting subsidence in the Cilicia Basin.

Model results

Model results portray the evolution over millions of years of a characteristic subduction wedge with forearc high (Fig. 2; Fig. DR3 and video DR1). Results simulate the growth of an accretionary wedge at a rate determined by a convergence velocity vc = 35 mm/yr and an accretionary thickness h = 3 km, i.e. an accretionary flux of 105 km^2/My. Sedimentation rate of Sed_r = 0.5 mm/yr occurs as the wedge grows until sediments fill depressions to capacity. Values of these and other parameters are chosen to match observations along the Central Cyprus transect (Fig. 1; Fig. DR3) after a simulation time of 25 My. In general, results scale such that the accretionary flux and run time trade-off at nearly one to one. Find details of the models in the Data Repository DR2.

Models show the typical morphologic elements of accreting subduction wedges with forearc highs (Fig. 2). North of the seaward migrating trench, the trench-slope wedge bounds a wide topographic depression that grows continuously as accommodation space is created by the landward increasing depth of the subduction slab. Steady infill of the forearc depression results in a negative-alpha basin that suppresses strain rates and

deformation of the underlying wedge (Fig. 2B). Temperature increases under the basin during its growth, resulting in a viscosity drop in the lower crust and ductile strain, which ultimately results in uplift of the forearc high and subsidence at seaward locations (Fig. 2C). At the end of the model run, subduction wedge accretion has led to elevated strain rates and widespread deformation from the trench to the forearc high. Subduction wedge accretion also results in wedge topography and wedge thickness continuously increasing landward until the forearc high, where topographic height is maximum.
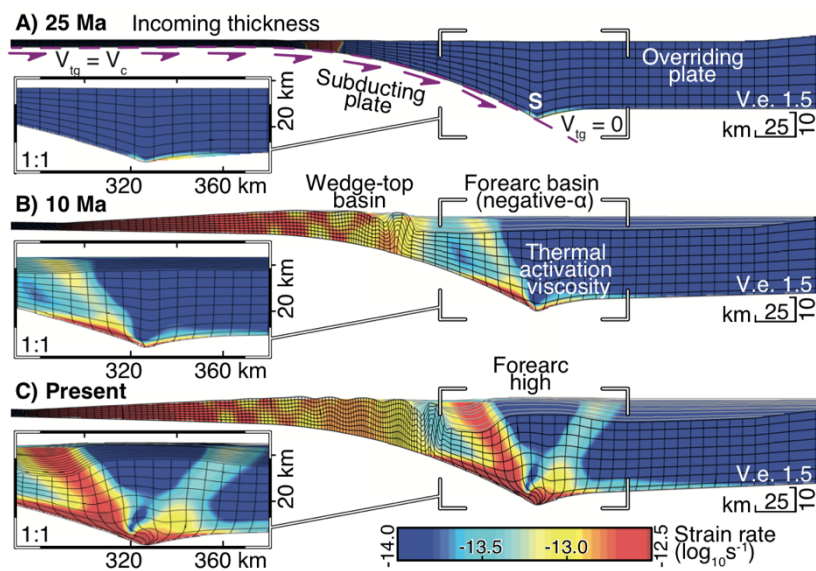

Figure 2. Three time-steps (initiation, ~10 Ma and present) in numerical thermo-mechanical model of viscous-plastic deformation for a convergent wedge undergoing basal traction to simulate subduction (see DR2). Insets are zoom-ins of the area where the forearc high develops at model scale. Color shows the second invariant of strain rate tensor, i.e. strain rate. Cumulative strain shown by the Lagrangian mesh. Individual lines on top of basement are isochrones (synthetic stratigraphy) that reflect the overall geometric relationships expected for strata. Upper panel represents the moment of subduction initiation at 25 Ma. Middle panel at 10 Ma show a wide forearc (negative-α) basin, increase in strain rate below it and wedge deformation reaching the future location of the forearc high. Bottom panel at present show a forearc high developed by a wide shear zone and onlaps in the synthetic stratigraphy above large strain rates at lower crust. See video DR1 in Data Repository.

Dynamic, thermo-viscous growth of forearc highs

Deep-seated flow (Pavlis and Bruhn, 1983) at the base of an orogenic wedge (Platt, 1986; Willett et al., 1993) provides a simple general framework to explain the formation of forearc highs. Crustal thickening by protracted wedge accretion increases the depth

of burial and the temperature of the lower crust (Willett et al., 1993). Synorogenic sedimentation developing the forearc basin similarly contributes to wedge thickening, and also raises lower crustal temperatures by increasing the thermal gradient underneath the basin (Fuller et al., 2006). Thermal resistivity of sediments leads "thermal blanketing" and increasingly higher temperatures in the underlying wedge as the basin grows, and ultimately results in the progressive change in the deformation mechanism from Coulomb friction to nonlinear viscous at the base of the crust. Lowering strength results in viscous flow at the base of the orogen and, given the compressional state of the wedge, it shortens horizontally and thickens, uplifting the forearc high (Fig. 2C). Thus, the forearc basin "thermal blanket" promotes deep-seated deformation that, in the context of accretion, propels the uplift of the forearc high while subsidence continues in seaward regions that are unaffected by viscous flow.

Discussion

The fundamental conditions required by the model presented here are quite simple. Accretion and syn-accretion sedimentation result in a progressive increase of crustal thickness in a subduction margin forearc. The increased thickness increases thermal resistance and Moho depth, thereby increasing lower crustal temperatures and changing deformation from frictional to viscous. We expect this process to take place in any accretionary system as it matures and increases in size, as for example documented on the Cascadia margin (Fuller et al., 2006; McNeill et a., 2000). Under protracted accretion and shortening, ductile strain in the lower crust switches vertical tectonic motions in the overlying wedge, from forearc basin subsidence to uplift, forming a new forearc high directly under the former basin (Fig. 3). Regions seaward, not affected by lower crustal flow continue to subside through sediment loading.

A viscous-flow controlled, structurally internal forearc high as we propose will form at a location determined by the geometry of the slab, and at a time determined by the accretion velocity, wedge temperature, and wedge viscosity. Thus, forearc highs are integral parts of accretionary wedges that may uplift in a dynamic, non-linear manner and become more probable as the accretion system matures. We note, however, that there are other mechanisms for the formation of a forearc high, including forced mechanical accretion against areas of relatively larger strength (Byrne et al., 1993) or changes in wedge taper or stress state (Willett and Schlunegger, 2010).

Sedimentation and sedimentation rate have other effects that control forearc high uplift. Sediment infill of the forearc topographic depression reduces the surface angle of the forearc wedge to zero and stabilizes the wedge underneath (Fuller et al., 2006). In addition, isostatic basin subsidence by sediment loading of the forearc persists seaward and landward of the uplifting forearc high. Hence, if the accretionary flux remains constant, variations in sedimentation rate control the localization of the forearc high uplift and potentially its uplift rate. This leads to the apparent paradox that regional subsidence in the forearc basin can control uplift in the forearc high for cases where sedimentation rate outpaces accommodation space, i.e. when subsidence controls the amount of sediment entering the system.

Our simulations are consistent with SCAP formation as a dynamic, thermo-viscous forearc high led by forearc sedimentation and accretion along Central Cyprus (Fig. 3). Models reproduce the growth of the SCAP, including the surface uplift of Central Taurides and coeval subsidence in the Cilicia Basin, resulting in the monoclinal flexure of Late Miocene rocks at the plateau margin scale (Fernández-Blanco et al., 2018), as well as the first-order upper plate strain along the Central Cyprus subduction zone (Figs. 1, 2 & 3). The Kyrenia Range trench-slope break divides the active frictional deformation in the seaward areas, resulting in wedge top basin of Messaoria, from the

landward negative-alpha Cilicia Basin and areas farther north, where thermally-activated viscosity in the deeper sectors of the wedge resulted in the uplift of the modern Central Taurides (Figs. 1C, 2C & 3B). In brief, compression led the mechanical, brittle, upper-crustal strain that developed the Cyprus forearc system, and also the thermal, ductile, lower-crustal deformation that propelled SCAP growth.
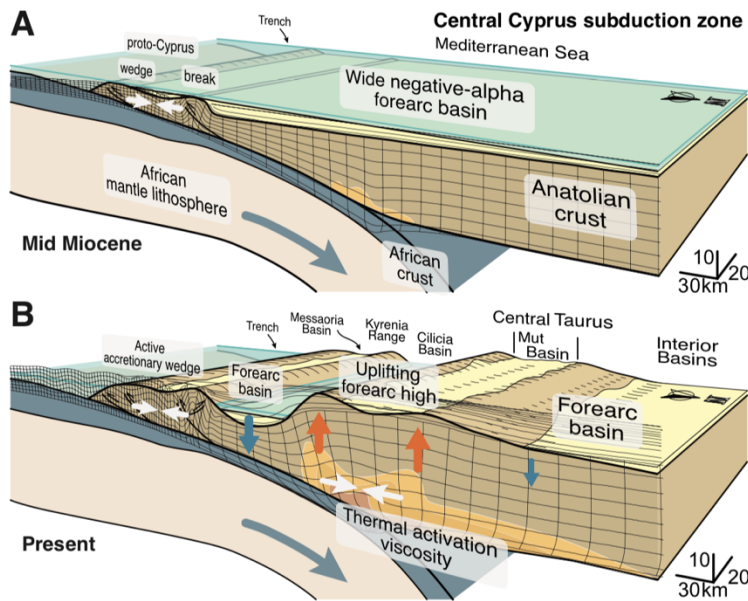

Fig. 3. Box model representation of the mechanism of thermo-viscous forearc high uplift in two time steps. Boxes show the evolution and forearc elements for a generic subduction wedge with forearc high and for the Central Cyprus margin. Time steps are interpreted as representative of the Central Cyprus margin. Integrated deformation is shown using the Lagrangian mesh of the model. Note that the model is only two-dimension.

The mechanism of dynamic, thermo-viscous forearc high growth provides a physical support for models of SCAP growth by contraction and crustal thickening (Fernández-Blanco et al., 2018; Meijers et al., 2018) that is at odds with models of epeirogenic surface uplift (e.g., Schildgen et al., 2014). Although our simulations can reproduce the dynamic growth of wider plateau-like terrains, the mechanism presented here cannot be responsible for the topography of the entire Central Anatolian Plateau, given the thin crust in the plateau interior (e.g., Abgarmi et al., 2017). As for the uplift of the plateau margin, evidence presented here point to single source growth accelerating in time (Fig. 2D, 3B). This mechanism is also compatible with disruption of the former forearc basin by uplift of the forearc high in Cascadia (McNeill et al., 2000), and suggests similar processes in the Alaskan, Nankai and Makran accretionary margins (Pavlis and Bruhn, 1983).

Conclusions

Simulations of subduction wedge accretion prove that thermally-activated viscous flow of the lower crust is a physically sound mechanism of forearc high growth. The model presented here provides a simple explanation of the complex space and time pattern of vertical motions in the central Cyprus/Anatolian subduction margin. We conclude that the plateau margin in South Turkey, and areas with a similar sequence of vertical motions in the interior of other accreting subduction wedges, grew as dynamic, thermo-viscous forearc highs.

Acknowledgments

References

Abgarmi, B., Delph, J.R., Arda Ozacar, A., Beck, S.L., Zandt, G., Sandvol, E., Turkelli, N., and Berk Biryol, C., 2017, Structure of the crust and African slab beneath the central Anatolian plateau from receiver functions: New insights on isostatic compensation and slab dynamics: Geosphere, v. 13, p. 1774–1787.

Aksu, A.E., Hall, J., and Yaltırak, C., 2005, Miocene to Recent tectonic evolution of the eastern Mediterranean: New pieces of the old Mediterranean puzzle: Marine Geology, v. 221, p. 1–13.

Allmendinger, R., Jordan, T., Kay, S., and Isacks, B., 1997, The evolution of the Altiplano-Puna plateau of the Central Andes: Annual Review of Earth and Planetary Sciences, v. 25, p. 139–174.

Bartol, J., and Govers, R., 2014, A single cause for uplift of the Central and Eastern Anatolian plateau? Tectonophysics, v. 637, p. 116–136.

Byrne, D.E., Wang, W.-H., and Davis, D.M., 1993, Mechanical role of backstops in the growth of forearcs: Tectonics, v. 12, p. 123–144.

Cosentino, D., Schildgen, T., Cipollari, P., Faranda, C., Gliozzi, E., Hudáčková, N., Lucifora, S., and Strecker, M.R., 2012, Late Miocene surface uplift of the southern margin of the Central Anatolian Plateau, Central Taurides, Turkey: GSA Bulletin, v. 124, p. 133–145.

Delph, J.R., Abgarmi, B., Ward, K.M., Beck, S.L., Arda Özacar, A., Zandt, G., Sandvol, E., Türkelli, N., and Kalafat, D., 2017, The effects of subduction termination on the continental lithosphere: Linking volcanism, deformation, surface uplift, and slab tearing in central Anatolia: Geosphere, v. 13, p. 1788–1805.

Fernández-Blanco, D., Bertotti, G., Aksu, A., and Hall, J., 2018, Monoclinal flexure of an orogenic plateau margin during subduction, south Turkey: doi: 10.17605/OSF.IO/KS6RG.

Fuller, C.W., Willett, S.D., and Brandon, M.T., 2006, Formation of forearc basins and their influence on subduction zone earthquakes: Geology, v. 34, p. 65–68.

Göğüş, O.H., and Pysklywec, R.N., 2008, Mantle lithosphere delamination driving plateau uplift and synconvergent extension in eastern Anatolia: Geology, v. 36, p. 723–726.

Göğüş, O.H., Pysklywec, R.N., Şengör, A.M.C., and Gün, E., 2017, Drip tectonics and the enigmatic uplift of the Central Anatolian Plateau: Nature Communications, v. 8, p. 1538.

McNeill, L.C., Goldfinger, C., Kulm, L.D., and Yeats, R.S., 2000, Tectonics of the Neogene Cascadia forearc basin: Investigations of a deformed late Miocene unconformity: GSA Bulletin, v. 112, p. 1209–1224.

Meijers, M.J.M., Brocard, G.Y., Cosca, M.A., Lüdecke, T., Teyssier, C., Whitney, D.L., and Mulch, A., 2018, Rapid late Miocene surface uplift of the Central Anatolian Plateau margin: Earth and Planetary Science Letters, v. 497, p. 29–41.

Molnar, P., 1984, Structure and Tectonics of the Himalaya: Constraints and Implications of Geophysical Data: Annual Review of Earth and Planetary Sciences, v. 12, p. 489–516.

Mutlu, A.K., and Karabulut, H., 2011, Anisotropic Pn tomography of Turkey and adjacent regions: Geophysical Journal International, v. 187, p. 1743–1758.

Pavlis, T.L., and Bruhn, R.L., 1983, Deep-seated flow as a mechanism for the uplift of broad forearc ridges and its role in the exposure of high P/T metamorphic terranes: Tectonics, v. 2, p. 473–497.

Platt, J.P., 1986, Dynamics of orogenic wedges and the uplift of high-pressure metamorphic rocks: GSA Bulletin, v. 97, p. 1037–1053.

Schildgen, T.F., Yıldırım, C., Cosentino, D., and Strecker, M.R., 2014, Linking slab break-off, Hellenic trench retreat, and uplift of the Central and Eastern Anatolian plateaus: Earth-Science Reviews, v. 128, p. 147–168.

Strecker, M.R., Alonso, R., Bookhagen, B., Carrapa, B., Coutand, I., Hain, M.P., Hilley, G.E., Mortimer, E., Schoenbohm, L., and Sobel, E.R., 2009, Does the topographic distribution of the central Andean Puna Plateau result from climatic or geodynamic processes? Geology, v. 37, p. 643–646.

Walsh-Kennedy, S., Aksu, A.E., Hall, J., Hiscott, R.N., Yaltırak, C., and Çifçi, G., 2014, Source to sink: The development of the latest Messinian to Pliocene–Quaternary Cilicia and Adana Basins and their linkages with the onland Mut Basin, eastern Mediterranean: Tectonophysics, v. 622, p. 1–21.

Willett, S., Beaumont, C., and Fullsack, P., 1993, Mechanical model for the tectonics of doubly vergent compressional orogens: Geology, v. 21, p. 371–374.

Willett, S.D., and Schlunegger, F., 2010, The last phase of deposition in the Swiss Molasse Basin: from foredeep to negative-alpha basin: Basin Research, v. 22, p. 623–639.

Yildirim, C., Schildgen, T.F., Echtler, H., Melnick, D., and Strecker, M.R., 2011, Late Neogene and active orogenic uplift in the Central Pontides associated with the North Anatolian Fault: Implications for the northern margin of the Central Anatolian Plateau, Turkey: Tectonics, v. 30, p. TC5005.

Data Repository DR1.

We reconstruct a transect spanning from the East Mediterranean to the Central Anatolian Plateau interior (Fig. 1B) interpreting the data shown in Fig. DR1, integrating it with the TransMED transect VII (Stephenson et al., 2004), and using constraints from Bakırcı et al. (2012) and Biryol et al. (2011) as appropriate. During data interpretation we focus on constraining the thicknesses of the African and Anatolian crust as well as the dip of the Cyprus slab. Crustal thicknesses along the transect range from a minimum of 25 km to a maximum of approx. 45 km. In the southern sectors of the transect, thickness changes are well detected by the gravimetric signal of Ergün et al. (2005) and the Moho models of Koulakov and Sobolev (2006). In the African plate, average crustal thicknesses of ~28 km are observed at the site of the Eratosthenes Seamount, south of Cyprus, and the African lithosphere is ~40 km thicker than northwards. The thinnest oceanic crust (25 km) is seen below the trench area. Northward and in an overriding position, thickening occurs in relation to the Troodos Ophiolite, which detachment depth is uncertain. This crustal thickening is probably the result of thrust doubling due to Troodos emplacement. The locked under-thrust of the Eratosthenes Seamount is underneath this location. The extent of the continental crust underneath the Troodos Ophiolite and the position of its transition to oceanic crust more to the north remains enigmatic. Between 34°30' N and 37° N, all geophysical models concur on a significant increase in Moho depth northwards, from some ~28 km to >40 km, which we correlate with subducting slab steepening (up to 40°). An overall subduction angle of 45° is observed until ~60 km depth at 36°30' N, where ~60° angles are reached as the slab deepens. This steepness fit appearances of the slab at ~300 km in the interior of Central Anatolia – see A-A section of Biryol (2011). In the southern regions of the overriding Anatolian plate, a relevant crustal thickening occurs below the Central Taurus. Thicknesses of the Anatolian crust decrease gently from circa 45 km (Luccio and Pasyanos, 2007) to values in excess of 35 km. For this interpretation, we used Pn tomography from Mutlu and Karabulut (2011) instead of gravity data (Özeren and Holt, 2010) that points to crustal thickness values up to 10 km thicker. Similarly, the overriding Anatolian lithosphere varies from ~110 km in the contact with the Cyprus slab to ~85 km at the northern tip of the transect.

To reproduce uppermost crustal structures and the geometry of Miocene and younger rocks (Fig. 1C), we integrate own findings (Fernandez-Blanco, 2014) with

published data in regional studies (Robertson, 1998a, 1998b; Stephenson et al., 2004; Harrison et al., 2004; Calon et al., 2005a, 2005b; Çiner et al., 2008; Fernández-Blanco et al., 2013, 2018; McCay et al., 2013). We assembled the interpretations of each area as shown originally in their sources, and the reader is referred there for details.

Data Repository DR2.

Accretionary wedges at convergent margins and their associated forearc systems are mechanically analogous to a wedge of sand piled upfront a bulldozer, where the behavior of the taper angle between the surface slope and the basal dip is described by the critical wedge theory (e.g., Davis et al., 1983; Dahlen, 1984; Willett, 1992; Wang and Davis, 1996). For a given set of wedge mechanical properties (internal friction angle, basal friction, pore fluid pressure, cohesion), the taper angle is constant and the wedge grows self-similarly as new sediments accrete at its toe (e.g., Dahlen, 1984). If the taper angle becomes larger than critical, the wedge attains stability by displacing deformation toe-wards (sea-wards) whereas if the taper angle is smaller than critical, the wedge surface gains steepness to achieve the critical taper angle.

1. The numerical code

We used an improved version of the finite element numerical method described in Fuller et al. (2006a,b) to describe the relationship between the taper angle of the wedge and the mechanical properties of the accreting sediments. The method accounts for features associated with a subduction wedge, such as accretion of a relatively thin sedimentary layer and flexure of two elastic plates. The subduction process is simulated with a hybrid kinematic-dynamic method in which the subducting crust and mantle of both plates have a prescribed motion, and the crust of the overriding plate can deform in response to body forces and boundary velocities. This method can simulate the deformation of frictional materials, such as sand and rock, and has been verified against analytical solutions (Willett, 1992; Willett and Pope, 2004; Fuller et al., 2006a,b). The improved numerical method (Cassola, 2013) accounts for changes in sediment accumulation rate (compacted sedimentation rate) through time, strain softening/healing and material tracking.

The code obtains the numerical solutions for different parameters over two distinct domains (mechanical and thermo-kinematic domain) (Figure DR2). The deformations

are calculated in the mechanical domain using a two-dimensional, mixed finite element Arbitrary Lagrangian-Eulerian method (ALE), during which the velocity and pressure are treated as independent variables (Fullsack, 1995) (Figure DR2a,b). The ALE method combines a semi-fix Eulerian mesh (Figure DR2a) and free Lagrangian markers (Figure DR2b). The Eulerian mesh is fixed along the horizontal position but free on the vertical direction to account for surface processes, and calculate the strain and stresses. The Lagrangian markers are free to move over the Eulerian mesh to compute the velocities and track the internal friction angle (ϕ) and the cumulative second invariant of the strain rate ($E_{2D}^{\frac{1}{2}}$). The temperature field is calculated on a thermal-kinematic domain using a Eulerian semi-fixed grid that includes as well the mechanical domain and covers the entire model from the base of the lithosphere to the surface (Figure DR2c) (Willett and Pope, 2004).

1.1. Strain, stress, and temperature

The strain is defined as the second invariant of the deviatoric strain rate (*I'2*). The resulting stress regime for each time step is calculated on the Eulerian mesh using the mean weighted value of the internal friction angle (ϕ) that is stored on the Lagrangian markers of each Eulerian element. Rheologically, the crustal domain is assumed to behave as an incompressible viscous fluid, with a frictional-depended plastic behavior and a thermally-activated viscous behavior. Frictional plastic deformation is calculated using a non-linear viscous formulation that approximates the limit condition associated with a Coulomb yield criterion. Temperature is determined within the thermal-kinematic domain solving a time-dependent heat transport equation, described in detail in Willet and Pope (2004) and including conduction, advection, and radiogenic heat production. The code resolves heat advection by dynamic calculus of the velocity in the mechanical domain and using a kinematically prescribed velocity elsewhere. The thermal parameters used can be found in Fuller et al. (2006) and an extended description of the equations are in Cassola (2013).

1.1.1. Strain softening

Strain is accommodated by brittle deformation in the crust (mechanical domain). In nature, this is expressed as a fault zone characterized by an embedded zone of weaker

material occurring during deformation and increasing strain (Rutter et al., 2001). A strain softening function (Cassola, 2013) in the numerical code reproduces the weakening of the rock with increasing strain. Numerical strain softening reduces the internal friction angle (ϕ) with increasing cumulative strain (Huismans and Beaumont, 2002) and is able to create localized shear zones. The strain rate for each time step, calculated on the Eulerian element, is added to the cumulative strain stored on the Lagrangian marker. The cumulative strain will be used then by the strain softening function to reduce accordingly the internal friction angle stored on the Lagrangian marker (Cassola, 2013).

The strain softening function used in the numerical model is based on the work of Frederiksen and Braun (2001):

$$\phi^* = B\phi + (1 - B)/E_k \qquad (1)$$

where

$$B = \frac{1}{2}\left[1 - \frac{2}{\pi}\arctan\left(\frac{E_{2D}^{\frac{1}{2}} - E_{crit}}{\Delta E}\right)\right] \qquad (2)$$

$$E_{2D}^{\frac{1}{2}} = \int_{t_0}^{t_{tot}} I'_2 dt - \int_{t_0}^{t_{tot}} E_{healing} dt \qquad (3)$$

The internal friction angle of the material, ϕ, is weakened to ϕ^* following an arctangent formulation where $E_{2D}^{\frac{1}{2}}$ is the cumulative second invariant of the deviatoric strain rate (I'_2) at each time step (3). Three parameters control the weakening method (Frederiksen and Braun, 2001). E_k describes the size of weakening from an initial internal friction angle, ϕ, to the weakened internal friction angle, ϕ^*. E_{crit} defines the amount of cumulative strain at which strength is reduced by 50%. ΔE is the strain interval over which the reduction takes place. The softening parameters have been tuned to get distinct weak shear zones.

1.1.2. Strain healing factor

Fault zones in nature show strength recovery after a period of inactivity (Yasuhara et al., 2005). We introduce this process in our numerical model by a "healing factor" coefficient that describes how the cumulative strain should recover over time (3).

We define the healing factor, $E_{healing}$, as a constant amount to the strain rate of one order of magnitude smaller than the average strain rate occurring on the last active thrust fault. This amount is subtracted from the total accumulated strain at every time

step for each Lagrangian marker (3). In this manner, if no deformation occurs at the Lagrangian element, the total accumulated strain decreases and the element gains in strength again with every timestep as the internal friction angle (ϕ) increases. Contrarily, if deformation occurs, the healing factor becomes neglectable compared to the actual strain rate affecting the element.

1.2. Sediment accumulation rate

The model adds material from an outside source and there is no mass balance. Model controls on sediment accumulation rates allow the creation of overfilled or underfilled basins. Overfilled conditions are met when high sedimentation rates result in sediments reaching the lower bounding flank of a basin, which in turn determines the fill level. Contrarily, underfilled conditions occur if sediments do not reach one of the two flanks of the basin, as for example when the dynamically calculated subsidence rate is higher than the prescribed sedimentation rate.

The model identifies the lowest point of a depression between two flanks to calculate the corresponding fill height on the basis of the specified sedimentation rate. Points of the Eulerian grid between the flanks that are below the fill height are then advected to the new fill level. The creation of new topography in the basin by the inclusion of the new sediments do not consider sediment compaction by overburden. Sediment rates are thus to be considered as already compacted sediment rates. At each time step, the simulation computes each sediment increment to calculate a new sediment load in the basin and a new isostatic load on the plates.

2. Model design

As explained above, our 2D kinematic-dynamic models consist of two coupled domains (Fig. DR3). Accretion of incoming sediments is driven by the tangential velocities at the base of the mechanical domain. These velocities decrease toward, and become zero at, the "S" point, which represents the point of contact of the subducting slab and the continental Moho. The thermal domain covers the whole model, including the mechanical domain.

The model is consistent with time and cross-sectional lengths of interest and simulates 25Ma of subduction in a transect of 550 km. Parameters such as amount of material incoming at the trench and convergence velocity are set constant during the

simulations. We adopted values of 3 km and 35 mm/y, respectively, which are considerably lower than present for the incoming material at the trench and higher than present for the convergence velocities. Our choice is based on the needed extrapolation in time (25 Ma) of present-day values. The present day sedimentary thicknesses in the East Mediterranean Sea range from 10 km to 15 km (e.g., Makris and Stobbe, 1984); these values are probably the largest along the time frame of interest, considering factors such as the narrower confinement of the present-day Mediterranean or the presence of the Nile. Similarly, the under-thrust of the Erastothenes Seamount below South Cyprus presently decelerates subduction motion to 9.3 ± 0.3 mm/y (Reilinger et al., 2006), thus a larger, more common, convergence velocity value is given for the time considered for our simulations.

The subducting lithosphere is 50 My old at the left side of the model and its 70 km thickness remains constant during the running time. Since thicknesses in the mechanical domain, which represents the crust, change as accretion takes place, an initial thickness of 30 km is chosen on the basis of the similarity between thicknesses in nature and in models after the run is completed, i.e., maximum values of 45 km near the "S" point. The rest of the overriding lithosphere is 80 km thick. Flexural rigidity is set at 2.4 x 10^{23} N·m for both plates (after Fuller, 1996). Variations of this value of up to four orders magnitude did not produce substantial changes (e.g., Forsyth, 1985 for a discussion on flexural rigidity values). Densities are commonly accepted values: 2.8 g/cc for the lithosphere (which includes the sedimentary cover), 3.3 g/cc for the mantle and 1.03 g/cc for the overlying layer of water. Cohesion and internal friction angles control the mechanical strengths in our model. Cohesion, c, is set to 1000 Pa, a value higher than expected for the crust, to maintain model stability. Lower values do not affect the outcomes (Fuller, 1996).

The internal friction angle of the crustal material, ϕ, is set to 27° and the friction angle between the subducting and the overriding plates, ϕ_b, to 8°. Friction values are set low to include the effect of fluid pressures, not explicitly taken into account, and imply fluid pressure ratios within the range of those at accretionary wedges (Fuller, 1996, and the references therein).

To let the thermal structure equilibrate, the thermal model runs for 20 My before the crustal model onsets. Surface temperature is 5 °C, an average between subaerial and subaquatic temperatures, and a value of 1400 °C is given for the asthenosphere at the

base of the model. We use values for thermal conductivity of 2 and 50 W/(m·°K) for the lithosphere and the asthenosphere. Asthenospheric conductivity values are readably high to represent isothermal conditions. Heat production has a value of 0.85 μW/ m^3 (Jaupart and Mareschal, 2005), occurring only in the mechanical domain. Specific heat, c, is 1200 J/ kg°·K for both model domains.

Data Repository References

Bakırcı, T., Yoshizawa, K., and Özer, M., 2012, Three-dimensional S-wave structure of the upper mantle beneath Turkey from surface wave tomography: Geophysical Journal International, v. 190, p. 1058–1076.

Biryol, C., Beck, S.L., Zandt, G., and Özacar, A., 2011, Segmented African lithosphere beneath the Anatolian region inferred from teleseismic P-wave tomography: Geophysical Journal International, v. 184, p. 1037–1057.

Calon, T.J., Aksu, A.E., and Hall, J., 2005a, The Neogene evolution of the Outer Latakia Basin and its extension into the Eastern Mesaoria Basin (Cyprus), Eastern Mediterranean: Marine Geology, v. 221, p. 61–94.

Calon, T.J., Aksu, A.E., and Hall, J., 2005b, The Oligocene-Recent evolution of the Mesaoria Basin (Cyprus) and its western marine extension, Eastern Mediterranean: Marine Geology, v. 221, p. 95–120.

Cassola, T. (2013). Mechanics of Forearc Basins. PhD thesis, Eidgenossiche Technische Hochschule (ETH).

Çıner, A., Karabiyikoğlu, M., Monod, O., Deynoux, M., and Tuzcu, S., 2008, Late Cenozoic Sedimentary Evolution of the Antalya Basin, Southern Turkey: Turkish Journal of Earth Sciences, v. 17.

Dahlen, F.A., 1984, Noncohesive critical Coulomb wedges: An exact solution: Journal of Geophysical Research, v. 89, p. 10125–10133.

Davis, D., Suppe, J., and Dahlen, F.A., 1983, Mechanics of fold-and-thrust belts and accretionary wedges: Journal of geophysical research, http://onlinelibrary.wiley.com/doi/10.1029/JB088iB02p01153/full.

Ergün, M., Okay, S., Sari, C., Zafer Oral, E., Ash, M., Hall, J., and Miller, H., 2005, Gravity anomalies of the Cyprus Arc and their tectonic implications: Marine Geology, v. 221, p. 349–358.

Fernandez-Blanco, D., 2014, Evolution of Orogenic Plateaus at Subduction Zones: Sinking and raising the southern margin of the Central Anatolian Plateau: PhD thesis, Amsterdam: Vrije Universiteit, http://dare.ubvu.vu.nl/bitstream/handle/1871/52042/end?sequence=3.

Fernández-Blanco, D., Bertotti, G., Aksu, A., and Hall, J., 2018, Miocene monocline flexure formed the

Central Anatolian Plateau southern margin:, Earth ArXiv doi: 10.17605/OSF.IO/KS6RG.

Fernández-Blanco, D., G., B., and and Attila, Ç., 2013, Cenozoic tectonics of the Tuz Gölü Basin (Central Anatolia Plateau, Turkey): Turkish Journal of Earth Sciences, v. 22, p. 715–738.

Forsyth, D.W., 1985, Subsurface loading and estimates of the flexural rigidity of continental lithosphere: Journal of Geophysical Research, v. 90, p. 12623.

Fuller, C.W. (1996). Controls on the Structural Morphology and Subduction Thrust Seismicity of Accretionary Margins. PhD thesis, University of Washington.

Fuller, C.W., Willett, S.D., and Brandon, M.T., 2006, Formation of forearc basins and their influence on subduction zone earthquakes: Geology, v. 34, p. 65–68.

Fuller, C.W., Willett, S.D., Fisher, D., and Lu, C.Y., 2006, A thermomechanical wedge model of Taiwan constrained by fission-track thermochronometry: Tectonophysics, v. 425, p. 1–24.

Fullsack, P., 1995, An arbitrary Lagrangian-Eulerian formulation for creeping flows and its application in tectonic models: Geophysical Journal International, v. 120, p. 1–23.

Harrison, R.W., Newell, W.L., Batıhanlı, H., Panayides, I., McGeehin, J.P., Mahan, S.A., Őzhűr, A., Tsiolakis, E., and Necdet, M., 2004, Tectonic framework and Late Cenozoic tectonic history of the northern part of Cyprus: implications for earthquake hazards and regional tectonics: Journal of Asian Earth Sciences, v. 23, p. 191–210.

Huismans, R.S., and Beaumont, C., 2002, Asymmetric lithospheric extension: The role of frictional plastic strain softening inferred from numerical experiments: Geology, https://pubs.geoscienceworld.org/gsa/geology/article-abstract/30/3/211/192319.

Jaupart, C., and Mareschal, J.C., 2005, Production from Heat Flow Data: The crust, v. 3, p. 65–84.

Koulakov, I., and Sobolev, S.V., 2006, Moho depth and three-dimensional P and S structure of the crust and uppermost mantle in the Eastern Mediterranean and Middle East derived from tomographic inversion of local ISC data: Geophysical Journal International, v. 164, p. 218–235.

Luccio, F., and Pasyanos, M.E., 2007, Crustal and upper-mantle structure in the Eastern Mediterranean from the analysis of surface wave dispersion curves: Geophysical Journal International, v. 169, p. 1139–1152.

Makris, J., and Stobbe, C., 1984, Physical properties and state of the crust and upper mantle of the Eastern Mediterranean Sea deduced from geophysical data: Marine Geology, v. 55, p. 347–363.

McCay, G.A., Robertson, A.H.F., Kroon, D., Raffi, I., Ellam, R.M., and Necdet, M., 2013, Stratigraphy of Cretaceous to Lower Pliocene sediments in the northern part of Cyprus based on comparative 87 Sr/86 Sr isotopic, nannofossil and planktonic foraminiferal dating: Geological Magazine, v. 150, p.

333–359.

Mutlu, A.K., and Karabulut, H., 2011, Anisotropic Pn tomography of Turkey and adjacent regions: Geophysical Journal International, https://academic.oup.com/gji/article-abstract/187/3/1743/618417.

Özeren, M.S., and Holt, W.E., 2010, The dynamics of the eastern Mediterranean and eastern Turkey: Geophysical Journal International, v. 183, p. 1165–1184.

Reilinger, R., McClusky, S., Vernant, P., Lawrence, S., Ergintav, S., Cakmak, R., Ozener, H., Kadirov, F., Guliev, I., Stepanyan, R., Nadariya, M., Hahubia, G., Mahmoud, S., Sakr, K., et al., 2006, GPS constraints on continental deformation in the Africa-Arabia-Eurasia continental collision zone and implications for the dynamics of plate interactions: EASTERN MEDITERRANEAN ACTIVE TECTONICS: Journal of Geophysical Research, v. 111, doi: 10.1029/2005JB004051.

Robertson, A.H.F., 1998a, Mesozoic-Tertiary tectonic evolution of the easternmost Mediterranean area: integration of marine and land evidence: Proceedings of the Ocean Drilling Program, Scientific Results, Vol. 160; Chapter 54, http://www.era.lib.ed.ac.uk/handle/1842/559.

Robertson, A.H.F., 1998b, Tectonic significance of the Eratosthenes Seamount: a continental fragment in the process of collision with a subduction zone in the eastern Mediterranean (Ocean Drilling Program Leg 160): Tectonophysics, v. 298, p. 63–82.

Rutter, E. H., Holdsworth, R. E., & Knipe, R. J. (2001). The nature and tectonic significance of fault-zone weakening: an introduction. Geological Society, London, Special Publications, 186(1), 1-11.

Stephenson, R.A., Mart, Y., Okay, A., Robertson, A., Saintot, A., Stovba, S., and Khriachtchevskaia, O., 2004, TRANSMED Transect VIII: Eastern European Craton--Crimea--Black Sea--Anatolia--Cyprus--Levant Sea--Sinai--Red Sea: The TRANSMED Atlas: The Mediterranean Region from Crust to Mantle, p. 120–127.

Wang, W.-H., and Davis, D.M., 1996, Sandbox model simulation of forearc evolution and noncritical wedges: Journal of geophysical research, v. 101, p. 11329–11339.

Willett, S.D., 1992, Dynamic and kinematic growth and change of a Coulomb wedge, *in* McClay, K.R. ed., Thrust Tectonics, Dordrecht, Springer Netherlands, p. 19–31.

Willett, S.D., and Pope, D.C., 2004, Thermo-mechanical models of convergent orogenesis: thermal and rheologic dependence of crustal deformation: Rheology and Deformation of the Lithosphere at Continental Margins. Columbia University Press, New York, NY, p. 179–222.

Yasuhara, H., Marone, C., and Elsworth, D., 2005, Fault zone restrengthening and frictional healing: The role of pressure solution: Journal of Geophysical Research: Solid Earth, v. 110, doi: 10.1029/2004JB003327.
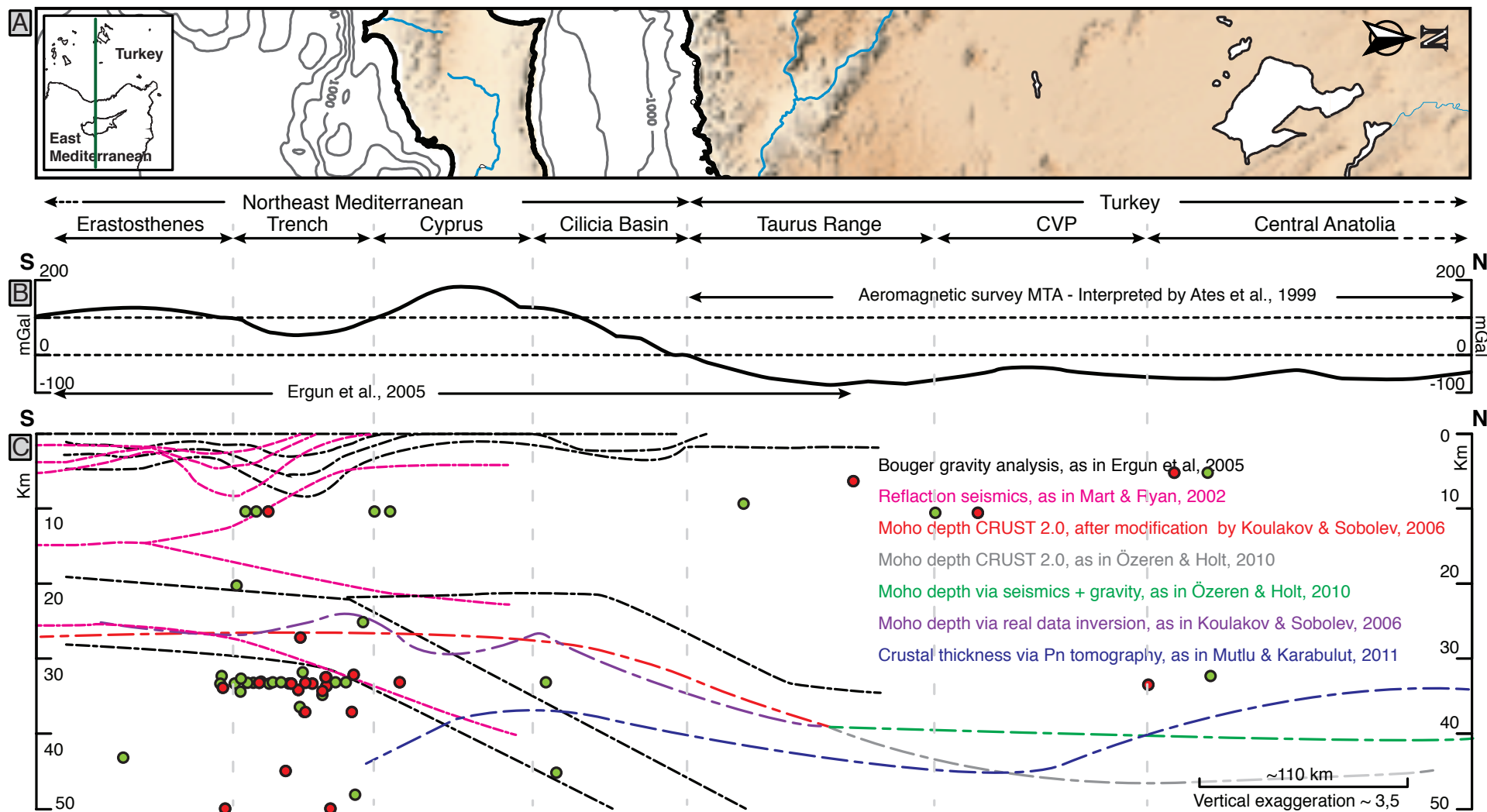
Suppl. Fig. DR1

Fig. DR1. A: Map view of a 2°-longitude wide (32°30'E to 34°30'E) swath running for ~650 km along latitude, used as reference for data along transects in panels B and C, located at its center. B: values along the section of interest derived from the two major gravimetric studies in the area (Ates et al., 1999; Ergün et al., 2005). C: published interpretation of the offshore section C in Ergün et al. (2005), and that of the seismic study performed by Mart & Ryan (2002), and several cross-sectional values along the section of interest derived from depth map models of the Moho (Koulakov and Sobolev, 2006; Özeren and Holt, 2010) and Pn tomography (Mutlu and Karabulut, 2011). The circles are focal epicenters with Mw> 5 recorded in a longitudinal area from 32°30'E to 34°E in red and 31°30'E to 34°30' E in green.
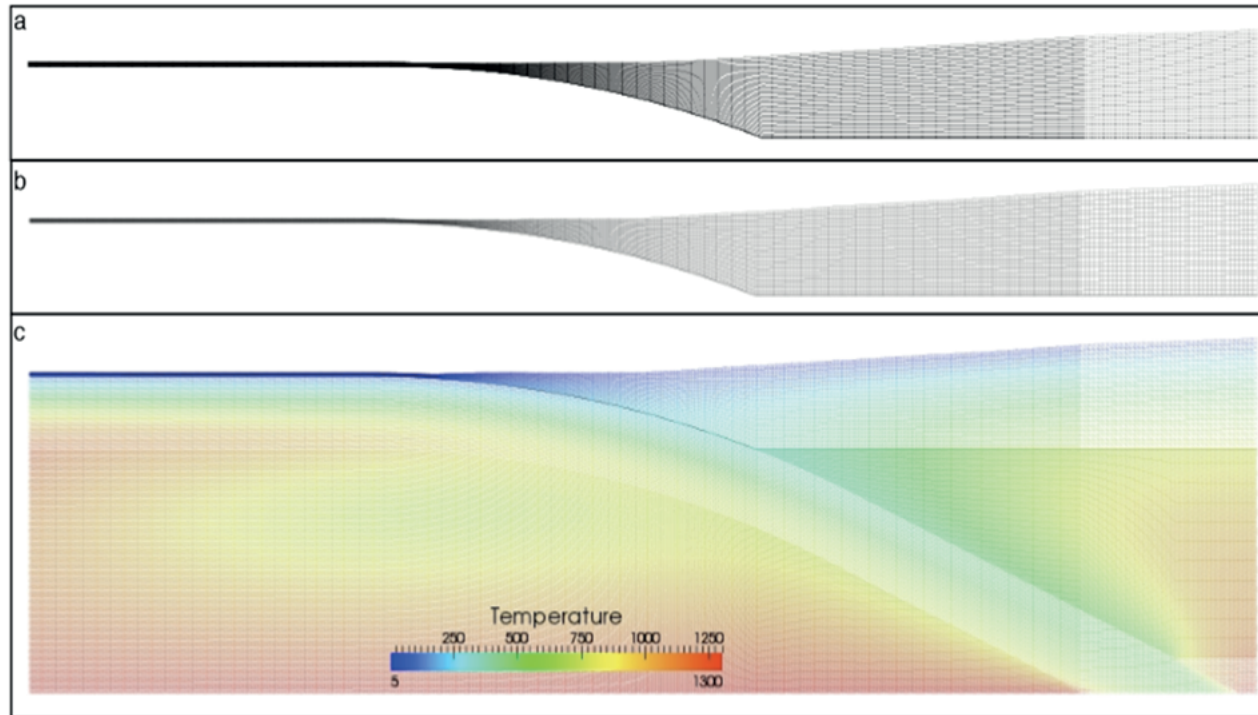
Suppl. Fig. DR2

Fig. DR2. ALE and thermal mesh used in the model. (a) Eulerian mesh, where strain, stresses, and velocities are calculated. (b) Lagrangian markers that advect over the Eulerian mesh in response to the calculated velocity and are used to track material properties, and the resulting weak zones. (c) Thermal domain, extending down to the asthenosphere. The temperature field calculated in the thermal domain is used in the mechanical domain to calculate thermally activated viscosity.
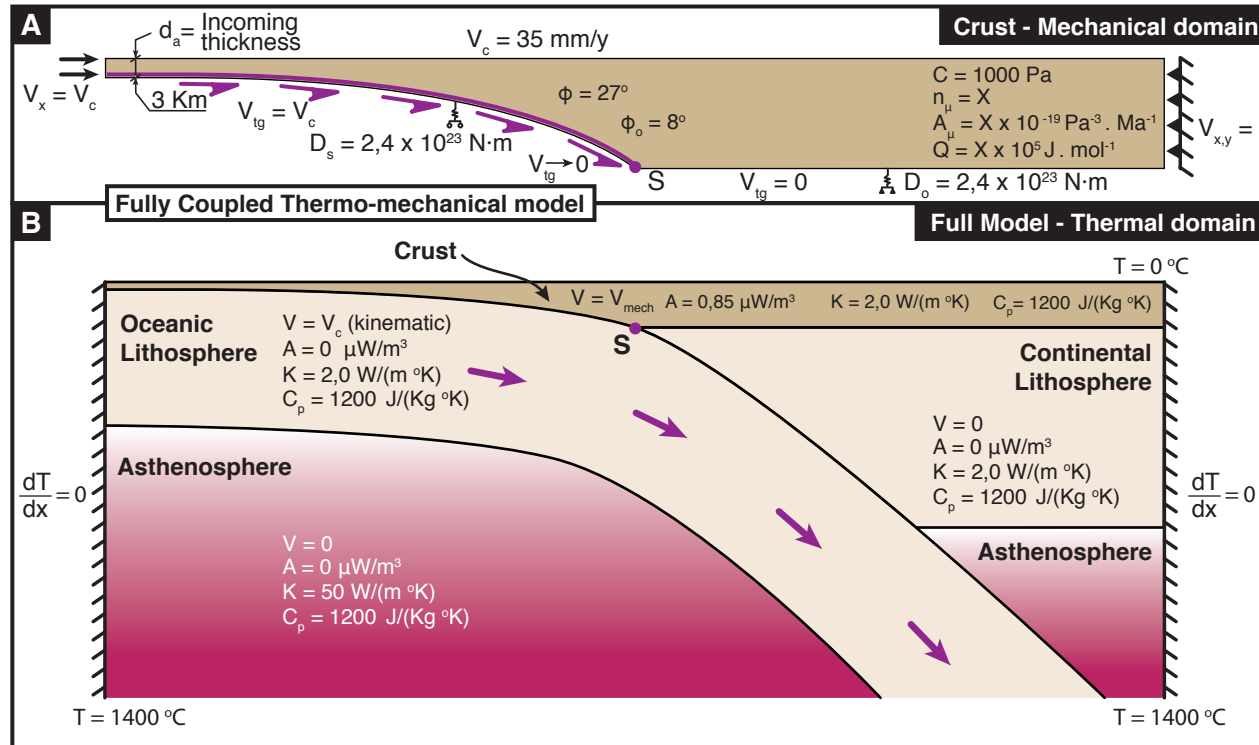
Suppl. Fig. DR3

Fig. DR3. Model set up, with indication of thermal and mechanical parameters.